REGISTRATION AND VISUALISATION OF DEFORMATION MAPS FROM TERRESTRIAL RADAR INTERFEROMETRY USING PHOTOGRAMMETRY AND STRUCTURE FROM MOTION

Rafael Caduff (rafael.caduff@geo.unibe.ch)

University of Berne, Switzerland

Gamma Remote Sensing AG, Gümligen, Switzerland

Dirk Rieke-Zapp (dirk.rieke-zapp@breuckmann.com)

Breuckmann GmbH, Meersburg, Germany

Abstract

This paper describes a general workflow for the registration of terrestrial radar interferometric data with 3D point clouds derived from terrestrial photogrammetry and structure from motion. After the determination of intrinsic and extrinsic orientation parameters, data obtained by terrestrial radar interferometry were projected on point clouds and then on the initial photographs. Visualisation of slope deformation measurements on photographs provides an easily understandable and distributable information product, especially of inaccessible target areas such as steep rock walls or in rockfall run-out zones. The suitability and error propagation of the referencing steps and final visualisation of four approaches are compared: (a) the classic approach using a metric camera and stereo-image photogrammetry; (b) images acquired with a metric camera, automatically processed using structure from motion; (c) images acquired with a digital compact camera, processed with structure from motion; and (d) a markerless approach, using images acquired with a digital compact camera using structure from motion without artificial ground control points. The usability of the completely markerless approach for the visualisation of high-resolution radar interferometry assists the production of visualisation products for interpretation.

KEYWORDS: compact digital camera, digital photogrammetry, geo-monitoring, interferometric radar, metric camera, structure from motion

INTRODUCTION

CHANGE DETECTION AND QUANTIFICATION of process rates is one major objective of geomorphological studies. Based on reliable, precise and rapidly acquired quantitative information about changes on the earth's surface, hazard assessment of various processes such as landslides, rockfalls or snow-related risks can be performed. Topography and

deformation is nowadays assessed by various high-resolution and high-precision techniques such as photogrammetry (Rieke-Zapp, 2010), lidar (Roncat et al., 2010) and spaceborne synthetic aperture radar (SAR) (Prati et al., 2010).

The use of spaceborne SAR for the detection of millimetre-scale deformation of the earth's surface has been shown for several cases. Large areas suffering surface deformation can be detected and quantified; for example, crustal deformation resulting from earthquake or volcanic activity (Hooper et al., 2007), subsidence (Strozzi et al., 2001), landslide activity (Herrera et al., 2011), distinct subsidence due to construction in urban areas (Tesauro et al., 2000), as well as applications including glacier flow and ice mechanics (Strozzi et al., 2008). The main limitations of the technique are concerned with the precise determination of the orbital parameters of spaceborne sensors, such as relatively long revisit times (35 days for ERS, 11 days for TerraSAR-X), and the viewing geometry. These parameters have significant influences on the coherence of the interferometric observations and the line-of-sight (LOS) sensitivity for displacement measurements since radar interferometric observations detect only the component of deformation that is directed parallel to the LOS.

To overcome these limitations of spaceborne radar interferometry, several terrestrial radar interferometers have been developed over the last decade (Rudolf et al., 1999; Reeves et al., 2001; Aguasca et al., 2004; Werner et al., 2008), showing great potential for detecting and measuring continuous deformation of slopes in rugged terrains (Caduff et al., 2014). However, by changing the viewing geometry to that of a terrestrial observer, conventional georeferencing techniques may not be suitable anymore. This is often the case in near-vertical target areas such as steep slopes where landslides or rock wall instability processes occur. Because areas with increased hazard potential are often difficult or dangerous to access, a completely non-contact (remote) examination of the area as a first step is often indicated.

Fortunately, parallel to the development of terrestrial radar sensors, developments in computer vision have emerged as well, making it possible to easily process image sets taken with common compact cameras into 3D point clouds of the object (Snavely et al., 2006; Furukawa and Ponce, 2010). Studies showed that the accuracy of such models is reasonable for geo-scientific applications after proper referencing and scaling of the 3D point clouds (James and Robson, 2012; Remondino et al., 2012).

A registration of terrestrial radar interferometric data with terrestrial images has the advantage that it leads to a clear and intuitively understandable representation of deformation processes in the target area. These can be used by many people involved in the assessment of, for example, a high-risk situation without the need of special software products or a knowledge of the characteristics of radar image geometry. A similar approach for the visualisation of deformation measurements is presented by Manconi et al. (2013) using deformation information obtained by automated tacheometry. An additional advantage of this approach is that it eases the integration or fusion of data generated by different systems such as terrestrial hyperspectral imagery and terrestrial laser scanning (Kurz et al., 2011; Sima et al., 2014).

This paper describes the general concept of registering and fusing 2D terrestrial radar data with 3D point clouds from different image-based modelling methods (stereo-image photogrammetry and structure from motion) to compare their suitability for geocoding and visualisation of terrestrial radar data. An overview is provided of the general fusion concept from radar geometry to 3D point representation using an external digital elevation model (DEM) or point cloud. Finally, an accuracy assessment is performed of the different

methods for the re-projection of the data product onto the initial terrestrial photographs, for example, a LOS displacement map.

<div align="center">Terrestrial Radar Interferometry</div>

Radar interferometry allows precise detection and quantification of surface deformation using the phase differences of two observations made at different times (Caduff et al., 2014). Another product is provided by the generation of a 3D model of the sensed area using simultaneous acquisition of two spatially separated antenna positions (Noferini et al., 2007; Strozzi et al., 2012).

There are three main types of sensors used for terrestrial radar interferometry (TRI) currently available. A first sensor type (I) uses a real-aperture dish antenna to form a narrow beam in both the vertical and horizontal directions (pencil-shaped radar beam). A second type (II) also employs a real antenna, but is now focused only in the azimuth direction (fan-beam antenna). The third type (III) synthesises a narrow aperture by moving small horn antennas along a path during acquisition. With this approach, the wide beams of the horn antennas synthesise a wider aperture, thus overcoming resolution limitations due to the physical dimensions of the antennas used (SAR).

For system I, the vertical and horizontal angles are known from the dish positioning, and the mean distance to the scatter can be determined via the travel time of the signal; the absolute position of the scatterer in 3D object space is known. In both of the latter cases II and III, the vertical position cannot be resolved directly. Therefore, additional terrain information must be present to map the radar pixel representing the summed magnitude and phase of a radar footprint onto 3D object space.

Radar Image Characteristics

Information for each radar footprint of the received radar signal for the acquisition concepts II and III is available in a 2D image array. The information about the magnitude and phase of the radar echo is stored as a complex number. The size of the illuminated radar footprint in the range direction depends on the radar frequency bandwidth, in which the microwave signal is modulated to obtain the range distance via the travel time and the incidence angle of the radar beam along the LOS to the surface. The azimuth resolution depends on the range distance to the object and the physical properties of the antenna. In synthetic aperture radars it is defined by the path length of the antenna positions between the first and last occurrence of a distinct scatterer. For fan-beam antennas, the physical antenna size determines the horizontal beam angle while the beam width is inversely proportional to the physical length of the antenna. In this study a Gamma Portable Radar Interferometer (GPRI) was used (Werner et al., 2012), shown in Fig. 1(c). It is a real-aperture phase-coherent radar, using 2·06 m long fan-beam antennas (type II) with a beam width (aperture) of 0·4°, resulting in an azimuth resolution of about 8 m at a 1 km range distance. Image forming is done by rotation of the antennas around a vertical axis with sampling steps of 0·1° (azimuth oversampling); the nominal azimuth image resolution is therefore 2 m at a 1 km distance for surfaces perpendicular to the LOS.

Corner Reflectors

Radar imaging usually works with natural scatterers of the illuminated surfaces. However, for radiometric calibration of the backscatter image as well as for georeferencing
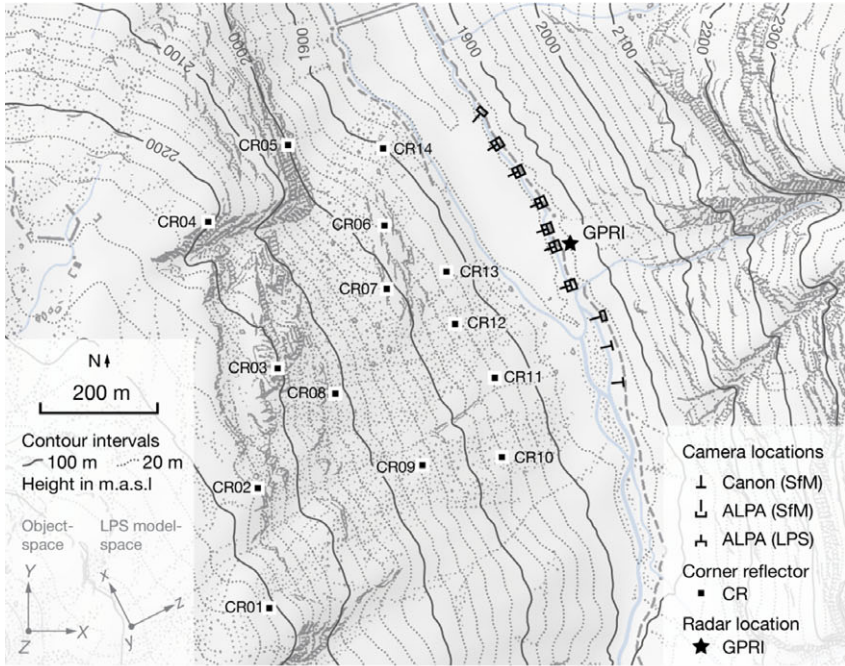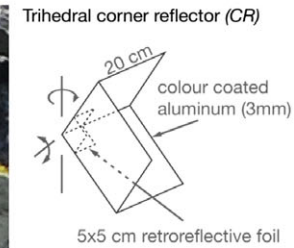
(a)
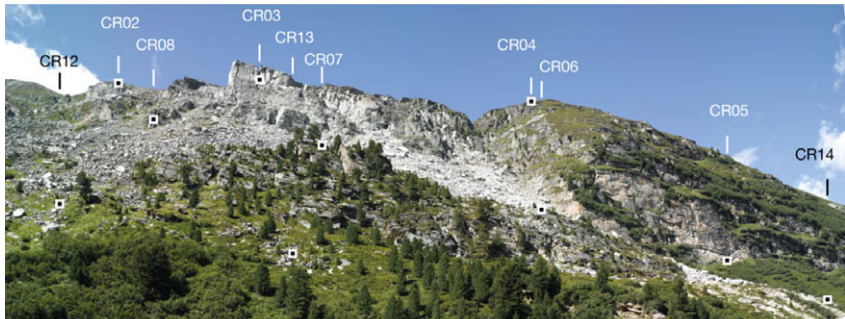
(b)

(c)

(d)

FIG. 1. Test site: (a) topographic overview; (b) terrestrial view of the area from the radar location; (c) terrestrial radar interferometer used for this study (GPRI: Gamma Portable Radar Interferometer); (d) corner reflector (CR) used as multi-use control points in the photographs and radar image.
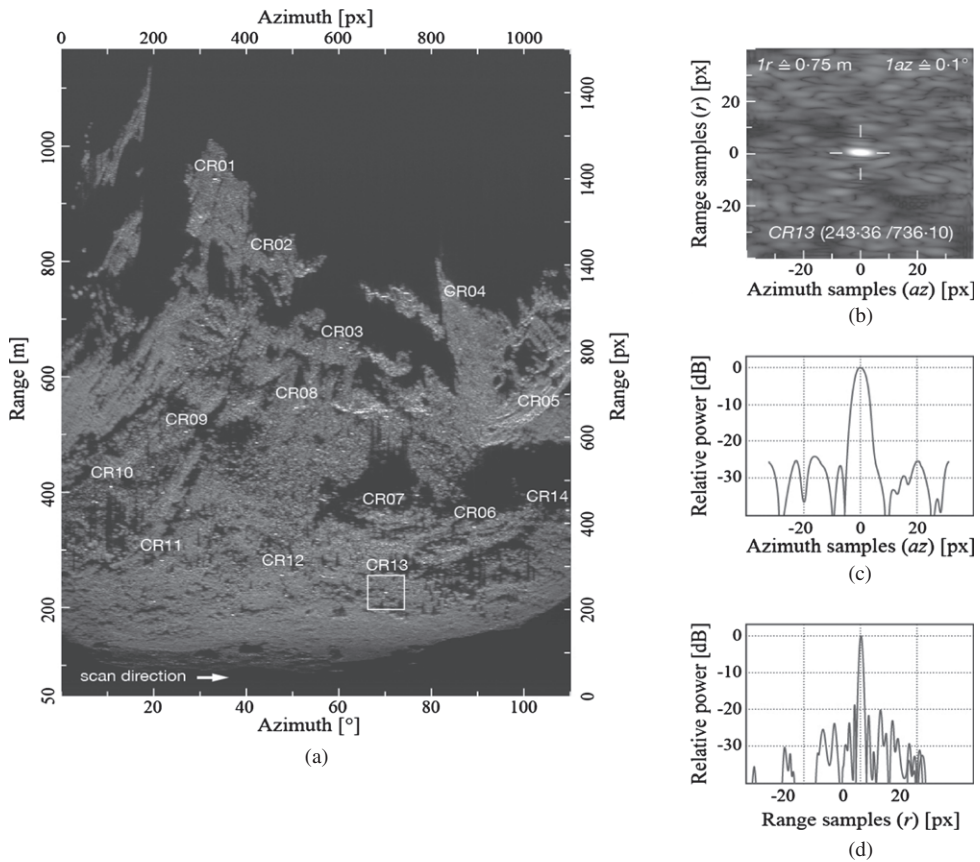
F_{IG}. 2. (a) Radar intensity image of the study site in polar radar geometry with indicated CR locations; (b) close-up of CR13 with sub-pixel location of the radiometric centre which was defined by determination of local maxima in azimuth (c) and range (d) profiles.

purposes, trihedral corner reflectors (CRs) (Fig. 1(d)) are often used for spaceborne and terrestrial platforms as well. The main advantage in using CRs for georeferencing purposes is that the radiometric centre in the backscatter image can be measured with sub-pixel precision (Fig. 2). The radiometric response of the targets is usually highly contrasted to the surrounding areas, which makes it stable over time even though the surrounding surface tends to decorrelate (for example, due to dense vegetation).

Current Radar Image Georeferencing Approaches

The nature of SAR and fan-beam radar systems does not allow a direct registration of a single radar pixel in 3D space due to the lack of information about the vertical position of a scatterer. Lingua et al. (2008) presented an approach for georeferencing radar data with the use of a geometrical transformation from the radar coordinate system to the object coordinate system. The transformation parameters are determined with control points of known coordinates. Tapete et al. (2013) further developed the approach of combining

terrestrial radar data with external high-resolution DEMs to produce an automated integration procedure. A combination of high-resolution elevation data such as point clouds obtained from terrestrial laser scanner (TLS) or surface models adds high value for the interpretation of findings made with radar data (for example, surface deformation). However, Manconi et al. (2013) showed that a simplified visualisation approach of surface deformation measurements using terrestrial red – green – blue (RGB) photographs simplifies the understanding of processes and the communication of the findings for non-geomatics specialists.

An alternative approach, namely, georeferencing the radar data using point clouds obtained from photogrammetric surveys, adds valuable high-resolution information for linking the radar data and 3D point clouds, together with the high information content and simplified access to information on terrestrial photographs. A reduction of the effort in the field for the collection of 3D point clouds (using a pocket camera instead of a heavy laser scanner), as well as a georeferencing approach without artificial marker points in the target area, would lead to a simplified acquisition and interpretation workflow.

EXPERIMENT WORKFLOW

The experiment was designed to compare the feasibility and accuracy of the registration of a 2D radar image to 3D point clouds determined by photogrammetry and structure from motion (SfM). Furthermore, the referenced information was back-projected onto the input images used for 3D reconstruction. Results were compared for four configurations: a photogrammetric approach with a metric camera (A); two SfM approaches using images taken with a metric camera (B) and a consumer-grade digital compact camera (C); finally, the feasibility of a complete markerless approach (D) with the compact camera was tested. The final visualisation of the radar data in the image geometry was compared quantitatively as well as qualitatively for the four different approaches.

The general workflow applied in this study is explained in this section step by step. A summarising workflow diagram can be found in Fig. 3.

Test Site Description and Experiment Set-up

The test site is located in Zervreila (Graubunden/Grisons) in the Central Swiss Alps on a rock and debris slope underlying various displacement mechanisms, such as frequent rock- and block-falls. Traces of a recent block-fall event in August 2010 are visible as the very bright areas in the centre of the image in Fig. 1(b). Total station measurements show movement of the whole rock mass where reflector CR03 is located, including the whole area 200 m north and south of CR03. Mean annual displacements are of the order of 0·20 m and locally exceeding 2·0 m after the block-fall event of August 2010.

Radar measurements used in this study were taken with the second generation Gamma Portable Radar Interferometer (GPRI-II) shown in Fig. 1(c). The instrument was positioned on a tripod at the location indicated on the map in Fig. 1(a).

The campaign with parallel acquisition of radar data and images for the photo-grammetric and SfM point cloud reconstruction took place on 12th August 2011. Images for the reference point cloud were taken with an ALPA 12 Metric camera (Leaf Aptus II 10 with 56 mm × 36 mm CCD sensor (9334 × 6000 pixels) and a Schneider Apo-Digitar 5·6/47 mm lens), where the principal point is offset by 8 mm for terrestrial applications (Rieke-Zapp, 2010). For comparison with the reference point cloud, images with a Canon Digital IXUS 60 digital compact camera (5·744 mm × 4·308 mm CCD sensor (2816 × 2112 pixels) with
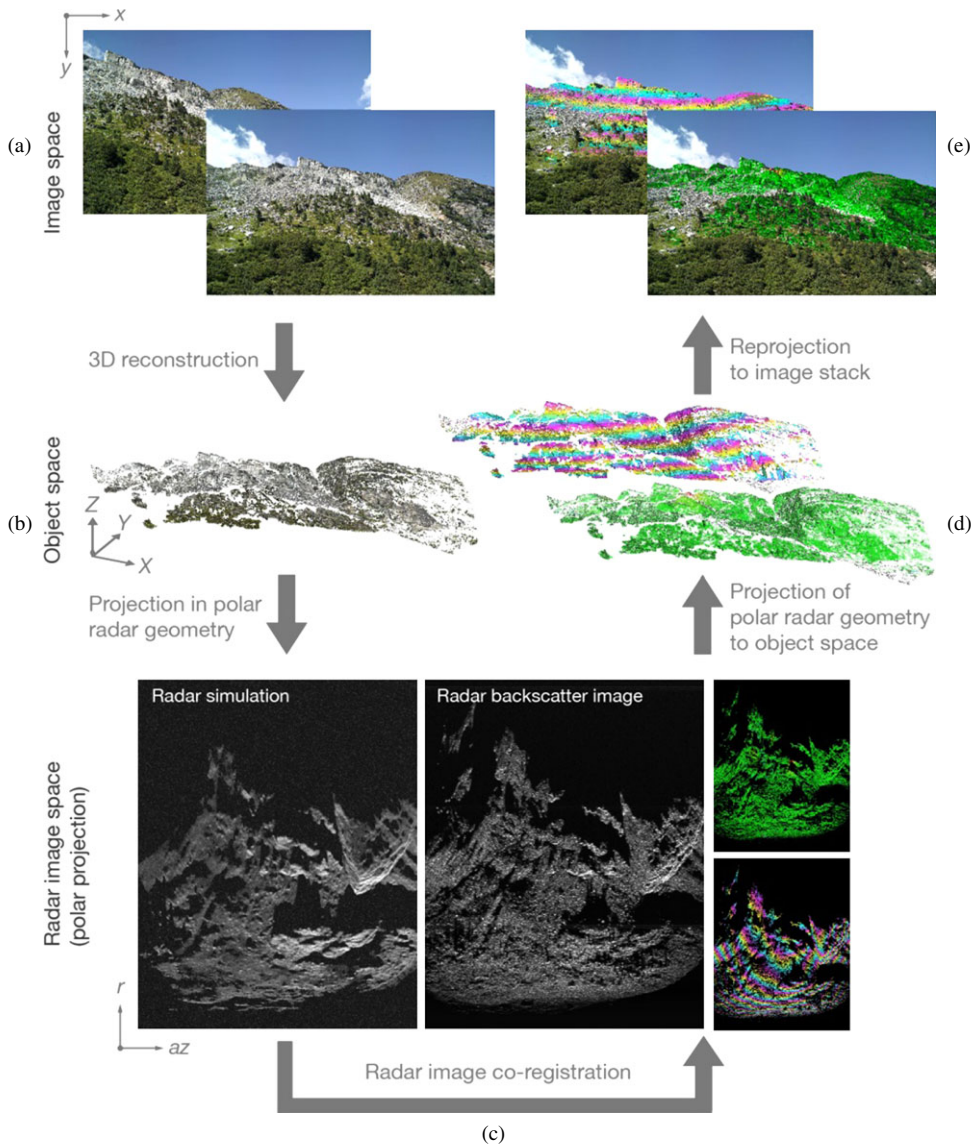
FIG. 3. Image-to-image workflow for the visualisation of radar data: (a) capturing of terrestrial photographs; (b) modelling and referencing of object points derived via stereo-image photogrammetry or SfM, together with the determination of intrinsic and extrinsic camera parameters; (c) simulation of radar intensities using object coordinates and co-registration of simulation and measured radar images; (d) linking the radar image to 3D object space; (e) re-projection and visualisation of final data product.

equivalent 35 to 105 mm lens) were taken at approximately the same photo locations. The locations and the average viewing directions are shown in Fig. 1(a). From these locations, the entire target area was acquired as image fans with an intended image overlap of 50%. Control points were visible from about 70% of the image locations. Images from the Canon

Digital IXUS camera were stored directly in JGEG format; images from the ALPA camera were processed from RAW to TIFF and JPEG formats for processing using SfM.

A total of 14 well-distributed CRs were installed as control targets over the entire test area that could be identified in the radar data as well as on the photographs. The locations of the targets are shown in Fig. 1. The trihedral CRs have an edge length of 20 cm, were colour coated for improved visibility in the photographs and equipped with retroreflective foil (three patches of 5 cm × 5 cm) at the corner of the reflector (Fig. 1(d)) for the determination of its 3D position using a Leica TCR803 Ultra total station.

3D Point Cloud Reconstruction from Images

The point cloud reconstructions from the images were performed in two different ways. The images taken with the ALPA metric camera were processed in the classical photogrammetric way using LPS 2010 from ERDAS in order to obtain a reference dataset for comparison with the outcome of the SfM approach. Images for the SfM approach were processed with Bundler v0·4 software from Snavely et al. (2006) in order to obtain the camera orientations and sparse point clouds, followed by a densification of the point cloud using PMVS2 from Furukawa and Ponce (2010).

(a) Stereo-image Photogrammetry. Extrinsic parameters and dense 3D point clouds were processed from the ALPA metric camera images using the intrinsic parameters from the previously applied calibration and the CR locations as ground control points (GCPs).

In order to facilitate photogrammetric processing with LPS, a transformation of the GCP coordinates from the Swiss national coordinate system (CH1903) has to be applied to an orthogonal right-handed reference system so that the *object Z* axis is almost parallel with the *image z* axis (terrestrial case). A seven-parameter transformation on the GCPs was applied and the processing of the data was performed with the use of these model coordinates. After completion, the results were back-transformed from *x*, *y*, *z* to *X*, *Y*, *Z* Swiss national coordinates (CH1903).

GCPs CR01, CR09, CR10 and CR11 were not used for the processing due to lack of visibility in the ALPA images. CR04, CR06 and CR13 were used as check points. The remaining seven CRs were used as GCPs. The residuals for the GCPs and check points are listed in Table I. Eleven images in total were used for the block triangulation. Three stereopairs with overlaps of between 83% and 91% were used for the point reconstruction. After merging point clouds derived from the stereo-image pairs, outliers and false points had to be removed from the point cloud. The final point cloud is shown in Table II.

(b) Structure from Motion. The ALPA dataset as well as the Canon IXUS dataset were fed, without specification of the principal distance (calibrated focal length) and lens distortion parameters, to the automated 3D reconstruction with the use of the SfM technique. All images in both datasets had to be scaled down (using a Lanczos filter) to image sizes of 2400 × 1543 pixels for the ALPA images and 2400 × 1800 pixels for the Canon IXUS images due to computation memory reasons. The result of the point reconstruction step is shown in Table II.
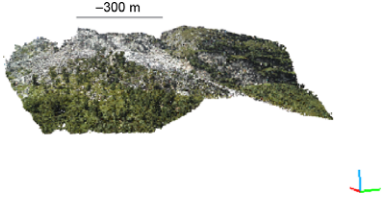
In a next step, the output point coordinates, currently in model coordinates which are neither oriented nor scaled, had to be transformed into *X*, *Y*, *Z* object coordinates. Both point clouds were transformed to object coordinates with the SfM Georef program (James and Robson, 2012) using the same GCPs and check points as for the ALPA/LPS approach.

Additionally, a markerless approach was performed on the Canon IXUS dataset using manually selected corresponding features in the SfM point cloud and an airborne laser

TABLE I. Georeferencing errors of point clouds.

	Control point RMSE [m]	Check point RMSE [m]	σ RMSE [m]	Minimum residual [m]	Maximum residual [m]
(A) ALPA Metric 12 using LPS	0·16	0·26	0·14	0·01 (CR12)	0·40 (CR04)
(B) ALPA Metric 12 using SfM Georef	5·10	10·65 (3·32 without CR04)	4·54 (1·76 without CR04)	2·05 (CR07)	17·83 (CR04)
(C) Canon Digital IXUS 60 using SfM Georef	0·77	1·77	0·75	0·40 (CR07)	2·86 (CR04)
(D) Canon Digital IXUS 60 using manual SfM	–	2·71	0·79	1·47 (CR03)	4·27 (CR02)

TABLE II. Point reconstruction results from the two image sets. The ALPA image dataset was processed with both the LPS and SfM approaches. In the bottom image (Canon IXUS) the outer faded area was excluded from the processing to match the extents in the upper two (ALPA 12) images.

ALPA 12 Metric

LPS processing

11 images

9334 × 6000 pixels

f = 47·376 mm (calibrated)

About 926 000 reconstructed points

ALPA 12 Metric

SfM processing

14 images

2400 × 1543 pixels

f = not fixed for SfM

About 96 000 reconstructed points

Canon Digital IXUS 60

SfM processing

130 images

2400 × 1800 pixels

f = 5 to 17 mm (uncalibrated)

About 849 000 reconstructed points

scanner (ALS) DEM reference dataset. The ALS reference dataset is available for the whole of Switzerland at a planimetric resolution of 2 m × 2 m (Swisstopo, 2004). A total of 27 features were identified and used for the determination of a seven-parameter transformation from model to object coordinates. All CRs were used as check points. The residuals of the check points are shown in Table I.

Radar Image Co-registration

The missing information about the vertical position of each scatterer in the radar images makes a mapping of the real-world coordinates to the radar image geometry necessary in order to create a lookup table for the back-projection. Therefore, the resulting four point clouds from the previous steps were used to simulate a 2D radar image. The simulation process used a simplified approach based on point location, point visibility and the relative radar footprint (number of points within a radar resolution cell together with local surface incidence angle) as sources for the simulated relative magnitude. The result is a greyscale image where the location as scatterers is plotted in polar projection (range/azimuth) with the same pixel sizes as the original radar image (0.75 m/$0.1°$). Finally, offsets (or, if present, block distortions of the initial point clouds) of the simulated and original radar images have to be corrected in a co-registration step using the methods outlined below.

The co-registration of the 2D representations of the reference point cloud (ALPA/LPS) and the Canon IXUS point cloud with the original radar image were performed using the sub-pixel locations of the CRs in the backscatter image and the calculated locations of the CRs in the simulated radar image. The calculated affine transformation parameters were also applied to the point cloud of the Canon IXUS using the SfM Georef program.

Due to significant residuals for the model-to-object coordinate transformation in the ALPA/SfM model when applying an affine transformation with the same parameters as for the ALPA/LPS approach, the transformation parameters were refined using natural common features in both the simulated radar image and the radar backscatter image.

To test the performance of a markerless approach without artificial GCPs, the final co-registration of the Canon IXUS/markerless model was performed with a six-parameter polynomial projection. To determine the polynomial coefficients, common features in the 2D representation and the original radar image were manually selected.

Radar Image to Point Cloud Projection and Photo Visualisation

Based on the co-registration of the simulated images and the radar image, every object point of the point clouds can now be referenced with the pixel value of its corresponding radar image location. Using the extrinsic parameters that were calculated for every image in the point cloud modelling step, it is possible to re-project the values linked with the object points to original image coordinates. The final projection of the colour information was linearly interpolated and overlaid on the corresponding image.

<div align="center">RESULTS</div>

The comparative error analysis was performed on the four cases (A, B, C and D) described. The object points from the reconstruction, whose projection lies in the radiometric centre pixel of the CR backscatter signal in the radar image, were re-projected onto all images of the initial image sets, taken close to the radar location (GPRI in Fig. 1). Due to the higher resolution of the point cloud compared with that of the radar, as well as possible effects of layover and foreshortening in the radar image, multiple object points can have their 2D representation in the same radar image pixel, marking the size of the radar footprint. Both the error ellipses (Fig. 4) of all the solutions of one radar resolution cell and the residuals of the ellipse centre to the CR centre in every image were calculated. An idealised appearance of the projection of a radar resolution cell is shown in Fig. 5 for comparison. Direct comparison of the various approaches (different image dimensions and scaling) was made possible by
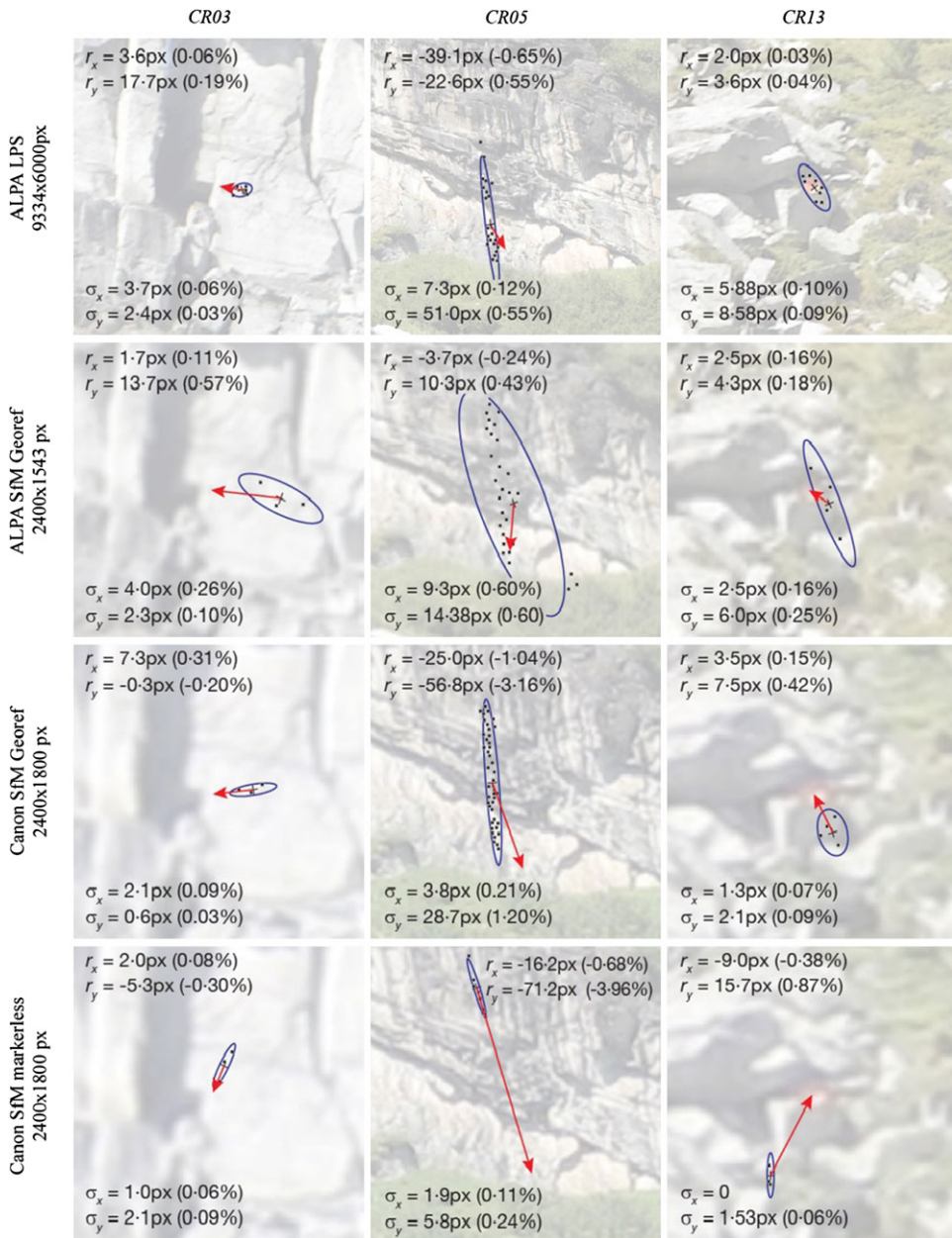
FIG. 4. Visual comparison of re-projections for the CR signatures used with the four different approaches (A to D).

stating the relative residuals as a percentage of the image dimensions used (see Fig. 4). The residuals of the same CR in different images of the subset were averaged and are shown in Table III.
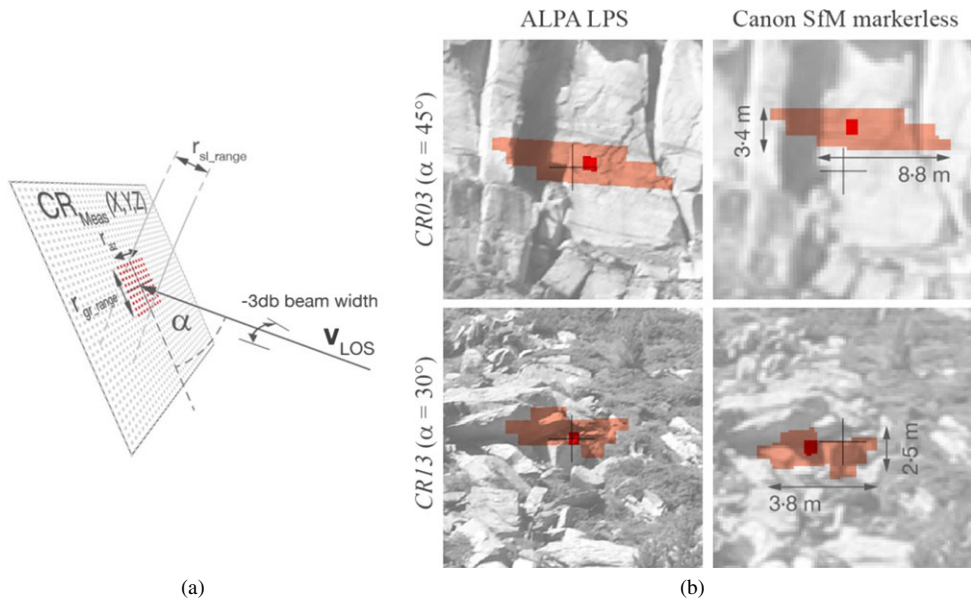
FIG. 5. Resolution of the radar image in object space. (a) Ideal flat surface showing the relationship between slant-range resolution r_{sl_range} along look direction $\mathbf{v}_{LOS}$ and ground-range resolution r_{gr_range} determined by the vertical incidence angle α. The horizontal incidence angle for this ideal surface is set to $90°$. (b) Range-dependent object resolution of the re-projections for approaches A and D using a flat representation from (a). The darker central rectangle corresponds to the radiometric centre pixel of the CR in the radar image. The surrounding irregular areas marked in a lighter hue correspond to the actual radar footprint of the CR signature. Range distances: CR03 = 660 m; CR13 = 230 m.

ALPA/LPS (Reference Model)

The reference point cloud created with LPS contained about 926 000 reconstructed points; this was after manual correction of false points that were particularly common in the densely vegetated areas on the lower parts of the slope. The root mean square error (RMSE) at the GCPs used ranged between 0·01 and 0·40 m. For comparison: the RMS in x, y, z of the total station measurements of the CR locations ranged between 0·01 m (CR12) and 0·08 m (CR01). After co-registration of the simulated radar image and the radar backscatter image, 7 out of 10 CRs could be re-projected onto the point cloud and therefore onto the initial image set. Points CR07, CR08 and CR14 could not be re-projected because no object point fell in the same location as the CR centre pixel. For the CR locations where object points could be determined, the residuals ranged between 0·04% and 0·45% (4·2 and 45·2 pixels) of the total image size. The maximum standard deviation (σ) is present in the projection of CR05 (σ_x = 7·3 pixels; σ_y = 51·0 pixels, corresponding to 0·08% and 0·85%, respectively).

ALPA/SfM

The dense point reconstruction of the down-scaled ALPA image set resulted in approximately 96 000 reconstructed points. The point density is about a tenth of the reference point cloud from the LPS approach. Patches where no, or only a few, points were

TABLE III. Radar-to-image projection errors in images taken close to the radar position.

Approach	A	B	C	D
Camera	ALPA Metric	ALPA Metric	Canon Digital IXUS	Canon Digital IXUS
Modelling approach	LPS + affine	SfM Georef + affine	SfM Georef + affine	SfM manual + polynomial
Image dimensions [pixels]	9334 × 6000	2400 × 1543	2400 × 1800	2400 × 1800
Number of images	4	4	11	11
	Mean residual [%]	*Mean residual [%]*	*Mean residual [%]*	*Mean residual [%]*
CR02	0·12	0·66	0·24	0·13
CR03	0·13	0·46	0·26	0·21
CR04	0·13	0·63	0·13	0·06
CR05	0·45	0·33	1·40	0·33
CR06	0·08	0·25	0·27	0·40
CR07	–[a]	0·10	0·78	0·14
CR08	0·09	–	0·23	0·41
CR12	–	–	0·43	0·09
CR13	0·04	0·12	0·39	1·15
CR14	–	–	0·33	0·36
Mean error	0·12	0·36	0·46	0·36
Total σ	0·09	0·24	0·42	0·41

[a]No corresponding point to centre pixel.

modelled are located where dense vegetation is present, especially bushes and trees. The georeferencing with SfM Georef led to RMSE values of 5·10 m for the GCPs and 3·32 m for the check points without CR04, which shows a RMSE of 17·83 m. The residual of CR04 is not in agreement with the results of the point cloud differences to the reference point cloud which ranged between 5 and 8 m in the surroundings of CR04.

The projection accuracies of the CR ranged between 0·10% and 0·63% (4·7 and 41·8 pixels) and led to a mean residual of 0·74%.

Canon IXUS/SfM/Georef

The result of the Bundler/PMVS2 point reconstruction from 130 input images led to a total of about 1 172 000 points. After cropping to yield the same extents as defined by the ALPA/LPS reference model (thus excluding the faded area in the bottom image in Table II) about 849 000 points remained. The initial image set contained a mix of images with different focal lengths ranging between 5·8 and 14·4 mm.

Scaling and referencing of the model to Swiss national reference frame CH1903 led to RMSEs of 0·77 m for the GCPs and 1·77 m for the check points; a maximum residual of 2·86 m was detected at check point CR04. The radar to object point referencing led to projection residuals ranging between a minimum of 0·13% (4·7 pixels) at CR04 and maximum of 1·40% (41·8 pixels) for CR05.

Canon IXUS/SfM/Markerless

The scaling and georeferencing of the point cloud was performed by the selection of matching topographic surface features in the model as well as in the reference ALS surface

model of the area. Using a total of 27 control points, the seven parameters were determined for the point cloud transformation. The projection applied to the CR was used to determine the RMSE of the transformation. The total RMSE was 2·71 m while the maximum error was 4·27 m at CR02.

Mapping the 2D radar image to the corresponding object points using an affine transformation led to average projection errors of 0·76% (25·5 pixels) while the maximum residual was 2·52% (81·8 pixels). The projection errors could be reduced to an average of 0·36% (10·5 pixels), with a maximum error of 1·15% (33·1 pixels) for CR13, using a six-parameter polynomial transformation instead of the affine transformation.

Projection of Radar Interferometric Results onto Images

Finally, the radar data were prepared for visualisation. The results of the ALPA/LPS and the Canon/SfM markerless approaches (A and D) are shown in Fig. 6. Prior to the visualisation of the radar data, a point projection of the available model points was created which is shown in Fig. 3(b). This allows control over whether the density of the points in the desired areas is sufficient for visualisation without further meshing and point densification.

The first dataset used for demonstration purposes is a single interferogram created from two single radar scenes taken at the same time but at spatially separated locations of the two receiving antennas. The vertical baseline is 0·25 m. The re-projection image in Fig. 6(c) shows the resulting fringes, while one colour cycle represents a phase shift of 2π radians at 17·2 GHz. Since the antennas are mounted parallel to one another and are horizontal, the fringe locations represent the same terrain heights.

A second information product is the high precision map of daily deformation rates, determined with an observation time of 12 h with a zero baseline. Displacement information was colour coded for the visible range. One small area with deformation rates of 2·5 mm per day is visible in the radar image (Fig. 3(c)). The location of this area in the images was possible after the projection on the terrestrial photographs (Fig. 6(d)). The same location is shown in both the ALPA/LPS and the Canon/SfM markerless images. The point density in this area is sufficient to show the distribution of the deformation. Field inspection and consultation of long-term total station data in this area confirmed the high deformation rates. This locality was the source of a major block-fall event in August 2010.

Discussion

The SfM reconstruction on 14 ALPA images resulted in a fairly sparse point cloud. In addition, large residuals in the georeferencing step are present. The low point density can be explained by the strong image down-sampling, necessary for the SfM reconstruction due to computation memory reasons. The initial images with 56 Mpixel resolution had to be scaled down to 3·7 Mpixel for processing using a quad-core 4 × 2·65 GHz processor with 8 GB RAM. The bundle block adjustment did not converge when the focal length was fixed; therefore, the calibrated focal length was used only as an initial value. The maximum offset from the individually calculated focal distances for each image to the calibrated and fixed focal length was 0·72 mm, thus resulting in a poor camera model. However, this can be seen as a direct consequence of the low number of input images together with the high down-scaling necessary for the processing, resulting in few matched homologous points. Since the camera model is poor, the georeferencing of the point cloud with seven GCPs only results in a very high RMSE.

Alpa LPS

Canon SfM - Markerless

(a)

(b)

0   2π
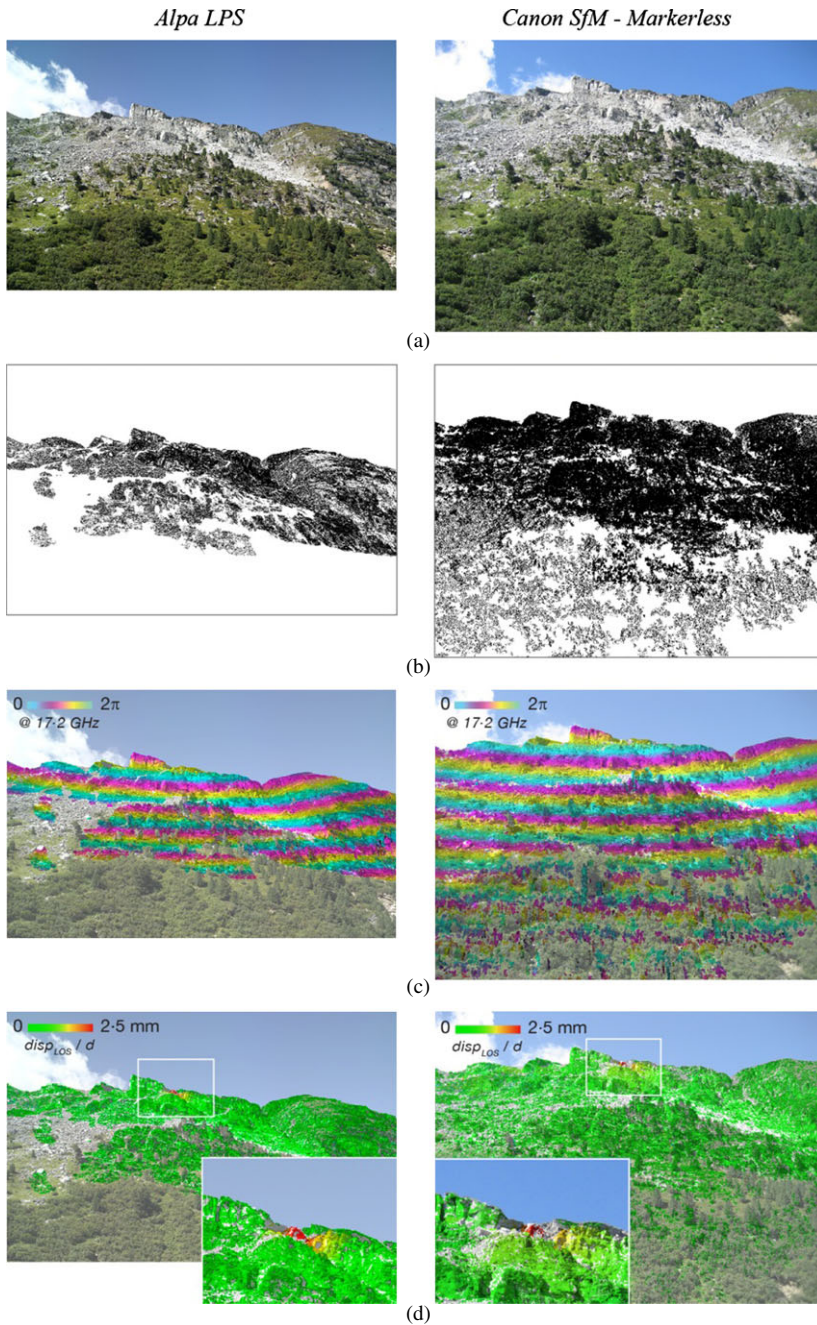@ 17·2 GHz

(c)

0   2·5 mm
$disp_{LOS}$ / d

(d)

Fig. 6. Re-projection results for images taken from radar location with the ALPA LPS approach A (left) and the Canon IXUS markerless approach B (right): (a) original images; (b) model point (black) distribution on the images; (c) projection of the interferometric height map (bi-static measurement with a vertical baseline of 25 cm); (d) projection of daily LOS displacement rates determined in a 12 h observation period (12th and 13th August 2011).

The final object-point densities for the ALPA/LPS and the Canon/SfM approaches are generally high. Lower densities resulted in areas with dense vegetation cover, especially at shorter distances. For the LPS approach, it was very hard to find matching points at such distances, since the stereo baselines of 30 to 100 m are not optimised for the close-range areas, while the depth of the target area ranges between 100 and 1000 m.

The georeferencing results for the ALPA/LPS approach yielded the best results as was expected. The more distant control and check points, that are up to 1000 m away from the camera, showed the highest residuals. The manual selection of the control points was difficult and not always successful since the pixel resolution at 1000 m is 0·12 m and the edge of a CR is 0·20 m long (Fig. 1(d)). All CRs were oriented directly towards the GPRI radar position to achieve the best radar reflectivity. Therefore, the selection of the centre of a CR from a side-looking position is difficult as well.

The georeferencing approach with SfM Georef for the Canon model resulted in a RMSE of 0·77 m for the control points and 1·77 m for the check points. This lies in the range of the ground sample distance in the down-scaled images of 0·80 m at 1000 m. Generally, the CRs could be located better in the Canon images because the acquisition of zoomed images of the CRs were contained in the initial image sets.

The registration, using a markerless approach for the co-registration of the Canon SfM model to object space, was achieved using a DEM with a resolution of 2 m × 2 m and a vertical accuracy of 0·5 m. The RMSE of the check points (all CRs were used as check points) was more than twice the RMSE of the SfM Georef approach. The residuals were not equally distributed over the area, which implies a non-uniform distortion of the markerless model. This distortion was present in the simulated radar scenes as well, so that a conventional affine registration of the simulation and the radar intensity image led to errors of several pixels. Due to the good distribution of natural marker points in the radar image, a six-parameter polynomial image transformation could be applied to overcome the substantial distortion after the markerless georeferencing. The back-projection of the CR locations onto the images resulted in even smaller errors than for the SfM Georef approach, therefore showing the importance and strength of reliable 2D co-registration of the simulated and the original radar backscatter image in order to overcome weak 3D point registration and block distortions in the point cloud. The residuals of the SfM markerless approach for the back-projection were of the order of three times larger than with the ALPA/LPS reference approach, but mostly less than the radar resolution, as shown in Fig. 5(b). The slant-range resolution (r_{sl_range}) depends on the system frequency; the azimuth resolution (r_{sl_az}) varies with the range and is defined by the physical or the synthesised length of the antennas and is therefore system dependent (Bamler, 2000). The GPRI specifications provide values for r_{sl_range} and r_{sl_az} of 0·8 m and about 8 m/km, respectively (Werner et al., 2012). The effective ground-range resolution is defined by the actual incidence angle from the LOS vector ($\mathbf{v}_{LOS}$) and leads generally to larger radar footprints than the theoretical maximum resolution defined by the system specifications. The effect on the resolution at vertical incidence angles close to 90° to the surface plane is visible for the back-projections for CR05 in Fig. 4. Since at this angle multiple points in the area fall in the same ranges (there is a large radar footprint), the vertical resolution is very poor and re-projections in such areas have to be interpreted very carefully. Since this effect has to be considered in advance during the radar campaign planning, such regions are generally excluded or even observed from other directions with better observation angles. Errors for the re-projection in such areas, therefore, reflect not only errors in the image registration but also the geometric effects of the radar acquisition.

The final re-projections (Fig. 6) show that the reduced effort and risk when installing GCPs in hazardous terrain for a completely markerless approach lead to comparable results to those achieved by the reference approach taken with terrestrial photogrammetry. However, in both cases it must be considered that information can be projected onto the images only at locations where 3D points were reconstructed. Necessary steps to ensure the reliability of the visualisations have to be made, such as for the quality control of the point reconstruction density, shown in Fig. 6(b). If the point density is insufficient, a densification of the point cloud can be achieved by surface meshing and point interpolation methods. Generally, as a rule of thumb, it can be said that the point cloud has to have at least the maximum radar resolution, which is likely to be $r_{\text{sl\_range}}$. Otherwise, it is possible that no projection solution is possible for certain areas, as occurred for certain points in the ALPA reconstructions (Table III).

Conclusion

This study has shown that the re-projection accuracy of range‒azimuth spaced radar information onto 3D point clouds created by terrestrial photogrammetry using the conventional approach is comparable to the ones created with completely markerless unguided SfM techniques. The overall accuracy is generally better than the size of the radar footprint.

However, to create reliable visualisations with markerless techniques, a reference DEM (from airborne or terrestrial laser scanning) of the area to be monitored has to be available; this DEM must exhibit reliable quality and its resolution must be of the order of the maximum radar image resolution. At the same time, the area must consist of several topographic features that make selection of natural control points possible for both the georeferencing from unstructured SfM model-to-object coordinates and for the co-registration of a radar simulation (based on the digital topographic model) to the measured radar image.

Limitations can be identified in the distribution and the density of the reconstructed object points. Usually point densities in strongly vegetated areas are much lower than on smooth rock surfaces with a high degree of colour texture. Additionally, the terrain roughness has an influence on the reconstruction result. In order to optimise the result of point matching, the user can influence the acquisition parameters. When dealing with rough terrain surfaces, the photographic baseline has to be small, resulting in small changes and therefore keeping the number of homologous points in the image high. A second optimisation of the process can be achieved by taking photographs in the same lighting conditions, thus avoiding strong contrasts.

Errors and distortions of the point cloud, referenced with a markerless approach using an external DEM, can be minimised by using a six-parameter polynomial instead of an affine transformation for the image co-registration of the simulated radar images and the measured radar backscatter image, but only if a sufficient number of natural tie points with a good distribution over the scene is present. Since for this approach only one SfM software package was used (without altering the initial parameters), improvements in the accuracies may be possible by using different parameters or different software solutions.

This research has showed the usability of SfM point clouds and camera calibration for the visualisation of 2D radar data on a set of terrestrial images. The visualisation helps to understand and locate areas of interest in the radar data from the observer viewpoint. This approach aids interpretation, especially in areas where the target area is not directly accessible due to imminent danger or due to the rugged nature of the terrain (such as steep

rock cliffs). However, since a necessary step in the visualisation is the 2D to 3D referencing of the radar image, 3D coordinates must be available as well. The final visualisation and referencing results can be of great value, for example, in the use of simplified data handling and distribution within the hazard assessment process where, usually, many people with different technical backgrounds are involved.

Acknowledgement

references

Aguasca, A., Broquetas, A., Mallorqui, J. J. and Fabregas, X., 2004. A solid state L to X-band flexible ground-based SAR system for continuous monitoring applications. *Proceedings of IGARSS Geoscience and Remote Sensing Symposium*, 2: 757–760.

Bamler, R., 2000. Principles of synthetic aperture radar surveys in geophysics. *Surveys in Geophysics*, 21(2–3): 147–157.

Caduff, R., Kos, A., Schlunegger, F., McArdell, B. W. and Wiesmann, A., 2014. Terrestrial radar interferometric measurement of hillslope deformation and atmospheric disturbances in the Illgraben debris-flow catchment, Switzerland. *IEEE Geoscience and Remote Sensing Letters*, 11(2): 434–438.

Furukawa, Y. and Ponce, J., 2010. Accurate, dense, and robust multi-view stereopsis. *IEEE Transactions on Pattern Analysis and Machine Intelligence*, 32(8): 1362–1376.

Herrera, G., Notti, D., García-Davalillo, J. C., Mora, O., Cooksley, G., Sánchez, M., Arnaud, A. and Crosetto, M., 2011. Analysis with C- and X-band satellite SAR data of the Portalet landslide area. *Landslides*, 8(2): 195–206.

Hooper, A., Segall, P. and Zebker, H., 2007. Persistent scatterer interferometric synthetic aperture radar for crustal deformation analysis, with application to Volcán Alcedo, Galápagos. *Journal of Geophysical Research: Solid Earth*, 112(B7): B07407. doi: 10.1029/2006JB004763

James, M. R. and Robson, S., 2012. Straightforward reconstruction of 3D surfaces and topography with a camera: accuracy and geoscience application. *Journal of Geophysical Research: Earth Surface*, 117: F03017. doi: 10.1029/2010JF002289

Kurz, T. H., Buckley, S. J., Howell, J. A. and Schneider, D., 2011. Integration of panoramic hyperspectral imaging with terrestrial lidar data. *Photogrammetric Record*, 26(134): 212–228.

Lingua, A., Piatti, D. and Rinaudo, F., 2008. Remote monitoring of a landslide using an integration of GB-InSAR and LIDAR techniques. *International Archives of Photogrammetry, Remote Sensing and Spatial Information Sciences*, 37(B1): 361–366.

Manconi, A., Allasia, P., Giordan, D., Baldo, M., Lollino, G., Corazza, A. and Albanese, V., 2013. Landslide 3D surface deformation model obtained via RTS measurements. In *Landslide Science and Practice, Volume 2: Early Warning, Instrumentation and Monitoring* (Eds. C. Margottini, P. Canuti & K. Sassa). Springer, Berlin, Germany. 690 pages: 431–436.

Noferini, L., Pieraccini, M., Mecatti, D., Macaluso, G., Luzi, G. and Atzeni, C., 2007. DEM by ground-based SAR interferometry. *IEEE Geoscience and Remote Sensing Letters*, 4(4): 659–663.

Prati, C., Ferretti, A. and Perissin, D., 2010. Recent advances on surface ground deformation measurement by means of repeated space-borne SAR observations. *Journal of Geodynamics*, 49(3–4): 161–170.

Reeves, B., Noon, D. A., Stickley, G. F. and Longstaff, D., 2001. Slope stability radar for monitoring mine walls. *SPIE*, 4491: 57–67.

Remondino, F., Pizzo, S. Del, Kersten, T. P. and Troisi, S., 2012. Low-cost and open-source solutions for automated image orientation – a critical overview. In *Progress in Cultural Heritage Preservation* (Eds. M. Ioannides, D. Fritsch, J. Leissner, R. Davies, F. Remondino & R. Caffo). *Lecture Notes in Computer Science*, 7616: 40–54.

RIEKE-ZAPP, D. H., 2010. A digital medium-format camera for metric applications – Alpa 12 Metric. *Photogrammetric Record*, 25(131): 283–298.

RONCAT, A., DORNINGER, P., MELZER, T., MOLNÁR, G., PFEIFER, N., SZÉKELY, B., ZÁMOLYI, A. and DREXEL, P., 2010. Effect of the acquisition geometry of airborne and terrestrial laser scanning on high-resolution outlining of microtopographic landforms. *EGU General Assembly Conference, Vienna, Austria*, 12: 15115.

RUDOLF, H., LEVA, D., TARCHI, D. and SIEBER, A. J., 1999. A mobile and versatile SAR system. *Proceedings of IGARSS Geoscience and Remote Sensing Symposium*, 1: 592–594.

SIMA, A. A., BUCKLEY, S. J., KURZ, T. H. and SCHNEIDER, D., 2014. Semi-automated registration of close range hyperspectral scans using oriented digital camera imagery and a 3D model. *Photogrammetric Record*, 29(145): 10–29.

SNAVELY, N., SEITZ, S. M. and SZELISKI, R., 2006. Photo tourism: exploring photo collections in 3D. *ACM Transacion on Graphics*, 25(3): 835–846.

STROZZI, T., WEGMÜLLER, U., TOSI, L., BITELLI, G. and SPRECKELS, V., 2001. Land subsidence monitoring with differential SAR interferometry. *Photogrammetric Engineering & Remote Sensing*, 67(11): 1261–1270.

STROZZI, T., KOURAEV, A., WIESMANN, A., WEGMÜLLER, U., SHAROV, A. and WERNER, C., 2008. Estimation of Arctic glacier motion with satellite L-band SAR data. *Remote Sensing of Environment*, 112(3): 636–645.

STROZZI, T., WERNER, C., WIESMANN, A. and WEGMÜLLER, U., 2012. Topography mapping with a portable real-aperture radar interferometer. *IEEE Geoscience and Remote Sensing Letters*, 9(2): 277–281.

SWISSTOPO, 2004. DTM-AV: Digitales Terrainmodell der amtlichen Vermessung. http://www.cadastre.ch/internet/cadastre/de/home/products/dtm_av.html [Accessed: 28th November 2011].

TAPETE, D., CASAGLI, N., LUZI, G., FANTI, R., GIGLI, G. and LEVA, D., 2013. Integrating radar and laser-based remote sensing techniques for monitoring structural deformation of archaeological monuments. *Journal of Archaeological Science*, 40(1): 176–189.

TESAURO, M., BERARDINO, P., LANARI, R., SANSOSTI, E., FORNARO, G. and FRANCESCHETTI, G., 2000. Urban subsidence inside the city of Napoli (Italy) observed by satellite radar interferometry. *Geophysical Research Letters*, 27(13): 1961–1964.

WERNER, C., STROZZI, T., WIESMANN, A. and WEGMÜLLER, U., 2008. A real-aperture radar for ground-based differential interferometry. *IGARSS Geoscience and Remote Sensing Symposium*, 3: 210–213.

WERNER, C., WIESMANN, A., STROZZI, T., KOS, A., CADUFF, R. and WEGMÜLLER, U., 2012. The GPRI multi-mode differential interferometric radar for ground-based observations. *EUSAR, 9th European Conference on Synthetic Aperture Radar*: 304–307.

Résumé

Cet article décrit une procédure de recalage entre des données radar interférométriques terrestres et des nuages de points 3D obtenus par photogrammétrie terrestre et par une technique de structure par le mouvement (SfM). Après la détermination des paramètres d'orientation internes et externes, les données obtenues par interférométrie radar terrestre sont projetées sur les nuages de points puis sur les clichés d'origine. L'affichage des mesures de déformation des versants fournit une information compréhensible et facile à communiquer, notamment dans le cas de zones inaccessibles comme des falaises ou des éboulis. Quatre approches de recalage et d'affichage sont comparées en termes d'aptitude et de propagation de l'erreur: (a) l'approche classique utilisant une caméra métrique et la restitution photogrammétrique d'images stéréoscopiques; (b) l'approche dans laquelle les images, acquises par une caméra métrique, sont traitées automatiquement par SfM; (c) l'approche dans laquelle les images, acquises par un appareil numérique compact, sont traitées par SfM; (d) l'approche dans laquelle les images, acquises par un appareil numérique compact, sont traitées par SfM sans points d'appui artificiels. Le potentiel de l'approche sans aucun point d'appui pour la visualisation des données radar interférométriques à haute résolution facilite la production de supports visuels pour l'interprétation.

Zusammenfassung

In diesem Artikel wird die Vorgehensweise für die Kombination flächendeckender 2D-Radarinter-ferometrie-Daten mit 3D-Punktwolken vorgestellt, die einerseits mittels klassischer Photogrammetrie und andererseits mit automatisierten "Structure from Motion" Technologien erstellt wurden. Die im Verlaufe der photogrammetrischen Analysen bestimmten inneren und äusseren Orientierungselemente können für die Visualisierung der Radar-Daten auf Bildernverwendet werden, die von derselben Position wie die Radar-Daten aufgenommen wurden. Die Limitierungen bezüglich Auflösung bei einer Darstellung von Aufnahmen in beinahe senkrechten Hängen und Felswänden, die bei einer klassischen Kartenprojektion entstehen, können mit dieser Darstellungsmethode umgangen werden. Ebenfalls wird durch den Gebrauch von Standard-Bildformaten die Kommunikation und Verteilung der Daten erleichtert. Es wird eine vergleichende Studie vorgestellt, die die Fehlerentwicklung bei den einzelnen Schritten aufzeigt. Es wurden (a) ein Referenzmodell, das mittels klassischer, Stereophotogrammetrie und einer Messkamera erstellt wurde mit den Resultaten aus "Structure from Motion"-Rekonstruktionen mit Bildern der (b) Messkamera und (c) einer handelsüblichen digitalen Kompaktkamera verglichen. Schliesslich wird auch die Machbarkeit einer Visualisierung mit einem (d) komplett berührungslosen Ansatz mit einer digitalen Kompaktkamera, der ohne Installation künstlicher Passpunkte auskommt präsentiert. Die Resultate zeigen, dass auch ein komplett berührungsloser Ansatz eine vergleichbare Abbildungsgenauigkeit wie die Referenzmethode hat. Dadurch lässt sich der im Feld getätigte Aufwand reduzieren, um Grundlagen für die Visualisierung zu schaffen.

Resumen

En este trabajo se describe un flujo de trabajo general para el registro de datos de interferometría de radar terrestre con nubes de puntos 3D derivados de fotogrametría terrestre. Después de la determinación de los parámetros intrínsecos y extrínsecos de orientación, los datos obtenidos mediante interferometría radar terrestre se proyectaron en las nubes de puntos y luego en las fotografías iniciales. La visualización de las mediciones de deformación del pendiente en las fotografías ofrece un producto de información de fácil comprensión y distribución, en especial de las zonas de difícil acceso, como paredes rocosas escarpadas o en las zonas de caída de rocas. La idoneidad y la propagación del error de los pasos anteriores y su visualización final se compara en cuatro aproximaciones: (a) la clásica utilizando una cámara métrica y la imagen estéreo fotogrametrica; (b) las imágenes adquiridas con una cámara métrica, procesadas automáticamente usando técnicas de estructura de movimiento; (c) las imágenes adquiridas con una cámara digital compacta, procesadas automáticamente usando técnicas de estructura de movimiento; y (d) una aproximación sin marcadores, utilizando imágenes obtenidas con una cámara compacta digital procesadas automáticamente usando técnicas de estructura de movimiento sin puntos de apoyo artificiales. La simplicidad de la aproximación sin marcadores para la visualización en alta resolución de la interferometría de radar ayuda a la producción de productos de visualización para la interpretación.

摘要

本文描述了一个针对地面干涉测量数据和从地面摄影测量手段或者从运动中恢复结构的三维点云数据配准的通用框架。对地面干涉测量数据经过内定向和外定向后，首先投影到三维点云，进而投影到影像上。这样对于在影像上边坡变形测量的可视化提供了一个易于理解和分发的信息产品。以下四种方法的参考步骤的适宜性和误差传播规律以及最终可视化效果得到了比较，第一经典的方法采用量测相机和立体摄影测量方式第二采用量测相机获取图像，采用运动恢复结构方式获得三维点云，第三,采用小型数码相机获取影像，采用运动恢复结构方式获得三维点云，第四,采用小型数码相机获取影像,在无控制点条件下采用运动恢复结构方式获得三维点云。针对第四种方案,可以辅助高分辨率雷达干涉测量结果的展示和解释。